RSC Advances

PAPER

View Article Online
View Journal | View Issue

Cite this: *RSC Adv.*, 2021, **11**, 30926

Highly sensitive optical temperature sensing based on pump-power-dependent upconversion luminescence in $LiZnPO_4:Yb^{3+}–Er^{3+}/Ho^{3+}$ phosphors†

Kamel Saidi, *[a] Wajdi Chaabani[b] and Mohamed Dammak [a]

In this work, various $LiZnPO_4$:0.5 mol% Ln^{3+} (Ln = Ho, Er) phosphors with different Yb^{3+} ion doping concentrations were synthesized by a sol–gel/Pechini method. X-ray diffraction (XRD) and scanning electron microscope (SEM) techniques were used to evaluate the phase and morphology of the samples. The UC process was mentioned as the typical emission peaks of Er^{3+} and Ho^{3+}. For Er^{3+} and Ho^{3+}, different optical temperature sensing methods are included. The Boltzmann distribution was accompanied by the fluorescence intensity ratio (FIR) for the two green Er^{3+} emissions originating from thermally-coupled levels. The effect of pump power on sensor sensitivities was extensively studied. The temperature uncertainty is also evaluated. The red and green emissions generated from non-thermally-coupled levels were used for temperature sensing in the Ho^{3+}-activated $LiZnPO_4$. High sensitivities were obtained in the phosphors, and the $LiZnPO_4:Yb^{3+}/Ho^{3+}$ showed the largest absolute sensitivities. $LiZnPO_4:Yb^{3+}–Er^{3+}/Ho^{3+}$ phosphors may be useful in the development of new luminescent materials for optical temperature sensing.

Received 10th August 2021
Accepted 13th September 2021

DOI: 10.1039/d1ra06049j

rsc.li/rsc-advances

Introduction

Temperature sensors account for 80% of the global sensor market, owing to their significance in a range of science and industrial applications.[1] Compared to traditional contact temperature measures like electrical resistance and thermocouples, which are constrained by reaction time and spatial resolution, non-contact thermometry approaches including Raman spectroscopy and luminescence are gaining traction.[2,3] The luminescence-based thermometry, in fact, has a number of benefits, including rapid response, high resolution and precision, and a wide temperature range.[4,5] Now, thermometry reliant on emission line intensity, bandwidth, spectral line direction, increase or decay life of the exciting polarization stage is used.[6–9] The most widely used technique is temperature-induced variations in luminescence intensity ratio (FIR) between two thermally coupled energy levels.[4,10] In particular, the lanthanide (Ln) particles doped upconversion (UC) phosphors are famously utilized for the FIR strategy. As it is well known, lanthanide ions have a unique electronic structure and are excellent discovery materials due to the advantages of their large Stokes decalage, their net emission profiles, and their long fluorescence lifetime.[11,12] The traditional activator ions for UC Luminescence (UCL) are Er^{3+}, Ho^{3+}, Tb^{3+} and Tm^{3+}.[6,13–15] Because of its large absorption portion about 980 nm, the Yb^{3+} ion is commonly used as a sensitizer to increase anti-stocks emissions.[16,17] On the basis of the rare-earth doped UCL materials, two strategies established to realize the FIR technique, containing thermally coupled levels (TCLs) and non-thermally-coupled levels (NTCLs). On the one side, two (TCLs) of activator ions are used, the populations of which obey the Boltzmann distribution, and their energy gaps are habitually in the range of 200–2000 cm^{-1}, such as Er^{3+}, Eu^{3+}, Dy^{3+}, Nd^{3+}, Mn^{4+} and so on.[18–24] However, since the energy gap between two TCLs is restricted, growing the relative sensitivity of an activator is hard. The second approach, which uses NTCLs of single or couple activators to overcome this problem, is being studied. Various luminescent ions of this class have been acquired, such Ho^{3+}, Pr^{3+}, and Tm^{3+}.[25–28]

On the basis of the above points, new luminescent materials with high-temperature sensor sensitivity need to be explored urgently. To develop new inorganic phosphor materials of more excellent temperature-sensing characteristics, continuous researches are still highly solicited. Apart from quantum dots and fluoride-based luminescent materials for optical temperature sensing.[29] In the previous reports, the properties of $LiZnPO_4$ phosphors doped rare-earth ions have been studied by

[a]*Laboratoire de Physique Appliquée, Groupe des Matériaux Luminescents, Faculté des Sciences de Sfax, Département de Physique, Université de Sfax, Sfax, BP, 1171, Tunisia. E-mail: saidikamel494@gmail.com*

[b]*Laboratoire de Physique des Solides, CNRS, Université Paris-Saclay, Orsay 91405, France*

† Electronic supplementary information (ESI) available. See DOI: 10.1039/d1ra06049j

some researchers.[30–32] To the best of our knowledge, the UC luminescence properties and optical temperature characteristics of Er^{3+}/Yb^{3+} and Ho^{3+}/Yb^{3+} in this host lattice have not been discussed so far, there has been no study into the Er^{3+} and Ho^{3+} activated $LiZnPO_4$ phosphors used for optical thermometry.

In this work, the $LiZnPO_4$ was chosen as the matrix due to its simple preparation, great physical stability, and environmental friendliness. The Er^{3+} and Ho^{3+} ions were used as the activators, and Yb^{3+} was employed as a sensitizer. The UC photoluminescence emission spectra excited by 980 nm NIR radiation and the sensitivities for temperature sensing were studied.

Experimental

Materials

To synthesize the $LiZnPO_4$ phosphors, we have used: lithium carbonate (Li_2CO_3, 99.5%, Rankem Reagent), zinc oxide (ZnO, 99.0%, Rankem Reagent), ammonium dihydrogen phosphate ($(NH_4)_2H_2PO_4$, 98.5%, E-Merck), erbium oxide (Er_2O_3, GR 99.99%), europium oxide (Ho_2O_3, 99.99%), ytterbium oxide (Yb_2O_3, 99.99%, nitric acid HNO_3 (69%).

Synthesis procedure

$LiZnPO_4$ nanosized phosphors were prepared by sol–gel method. The balanced method of the chemical composition and reaction used to prepare the host $LiZnPO_4$ from the starting material is as follows:

$$Li_2CO_3 + ZnO + (NH_4)_2H_2PO_4 \rightarrow 2LiZnPO_4 + 2NH_3\uparrow + CO_2\uparrow + 3H_2O$$

Firstly, the nitrates of all the oxides were obtained by dissolution in nitric acid. All solutions were added one by one in a glass beaker and kept for stirring at a constant rate. 0.1 M solution of polyethylene glycol (PEG) and citric acid solution were added to the above solution. The entire solution was kept for stirring and heating at 80 °C until the solution hydrolyzed into a sol and later on into a gel. The gel was kept for drying in an oven at 120 °C and the gel transformed into a dry dark brownish precursor. This procedure was followed for the preparation of all the phosphor samples in the series. The dark brownish precursors were transferred into porcelain crucibles and then heated in a muffle furnace at 600 °C for 1 h. Finally, it was put into alumina crucibles and burned in an electric furnace at the required temperatures for 3 h at 800 °C.

Characterization

The phosphors were measured in the 2θ range of 10–70° on an X-ray diffractometer (Bruker D8, Germany) with Cu Kα radiation (1.5405 Å), working at 40 kV and 30 mA for phase detection. The FT-IR spectrum for the titled compound was recorded at room temperature using a PerkinElmer Spectrum 1000 FT-IR spectrometer in the 400–4000 cm^{-1} range. A UV-vis-NIR spectrometer (PerkinElmer Lambda 950) was used to measure UV-vis-NIR absorption. The samples morphologies were studied using the Zeiss Supra 55VP SEM-FEG scanning electron microscope (SEM) with an accelerating voltage of 2–8 kV, equipped with a Bruker XFlash 5030 to study the elemental composition *via* energy dispersive X-ray spectroscopy (EDS). A JOBIN YVON HR 320 spectrometer with a temperature controller and a 980 nm laser excitation source was used to investigate temperature-dependent UC emissions. The sample temperature was controlled to be in the 300–440 K range by using a helium closed-cycle cryostat and a Lake Shore 321 temperature controller. The decay times were recorded on fluorescence spectrometer (Edinburgh FLS 980) equipped with a 980 nm laser source.

Results and discussion

XRD analysis

Fig. 1 exhibits the XRD patterns of the typical $LiZnPO_4$, $LiZnPO_4$:0.05% Er^{3+}/5% Yb^{3+}, $LiZnPO_4$:0.05% Ho^{3+}/3% Yb^{3+}. The standard XRD data of $LiZnPO_4$ were built with ICSD. The XRD pattern showed no additional peaks, suggesting that the prepared phosphors were produced in a single phase. These reflections show that the samples are well indexed to $LiZnPO_4$ and belong to a monoclinic process with the C_1c_1 space group.[33] The plane corresponds to the most extreme diffraction peak (004). Other important diffractions peaks are assigned at (311), (−223), (402), (204), (−225), (−330), (−516). The effective ionic radii of the Li^+, Zn^{2+}, P^{5+}, Er^{3+}, Ho^{3+} and Yb^{3+} ions are 102 pm, 74 pm, 38 pm, 89 pm, 94.7 pm and 86.8 pm respectively.[34,35] The dopant ions such as Er^{3+}, Ho^{3+} and Yb^{3+} are supposed to occupy the $LiZnPO_4$ lattice to substitute Zn^{2+} ions. There were no detectable impurities due to the low doping concentration.

Morphological analysis

Fig. 2a displays the morphology of a $LiZnPO_4$ powder sample. The slightly aggregated particles have irregular shapes and a small size range of 0.5–1 μm, which is favorable for enhancing its PL properties, which is also similar to the results obtained

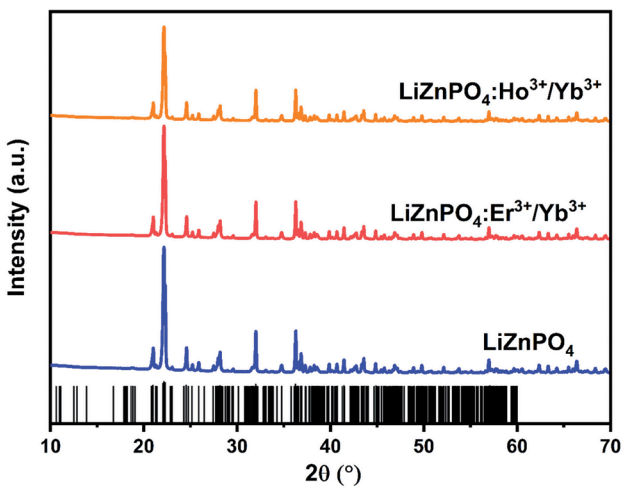

Fig. 1 XRD patterns of the $LiZnPO_4$, $LiZnPO_4$:0.05% Er^{3+}/5% Yb^{3+}, $LiZnPO_4$:0.05% Ho^{3+}/3% Yb^{3+}.

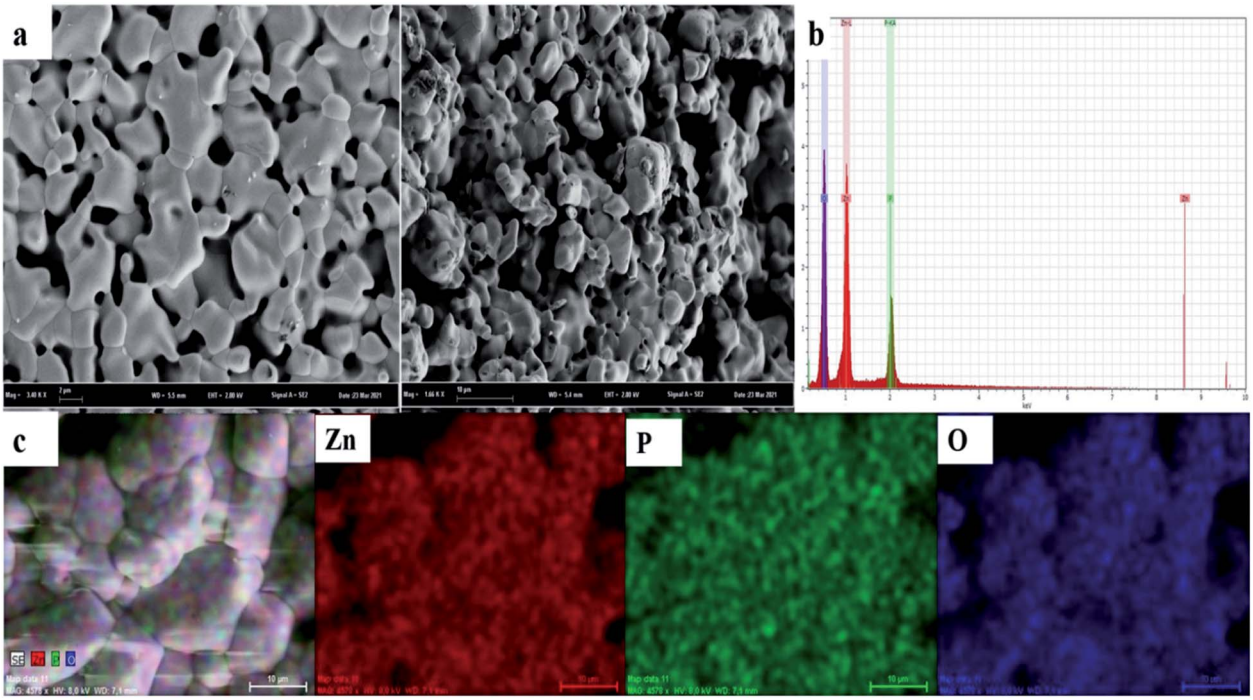

Fig. 2 $LiZnPO_4$ (a) SEM microscopic morphology image, (b) EDX spectrum, and (c) elemental mapping graphs.

for the sample $LiZnPO_4$:0.5% Er^{3+}/5% Yb^{3+} and $LiZnPO_4$:0.5% Ho^{3+}/3% Yb^{3+} in Fig. S1a and S2a† respectively. In addition, the elemental composition of a selected area shown in Fig. 2b is identified by the EDS elemental mapping and the results are represented in Fig. 2c. As can be seen, Zn, P, and O elements are uniformly distributed throughout the selected area. The light element Li was not detected in the all phosphors. To confirm the presence and relatively uniform distribution of Er^{3+}, Ho^{3+}, and Yb^{3+} element in the phosphors. The results of EDS spectrum and elemental mapping measurement of Er^{3+}, Ho^{3+}, and Yb^{3+} element in the phosphors is shown in Fig. S1 and S2,† which further confirms that the $LiZnPO_4$:0.5% Er^{3+}/5% Yb^{3+} and 0.5% Ho^{3+}/3% Yb^{3+} were successfully prepared and lanthanide ions have doped the host matrix uniformly.

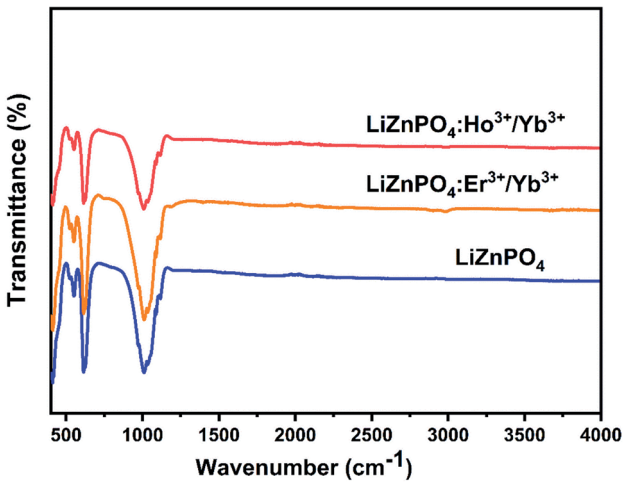

Fig. 3 FTIR spectra of $LiZnPO_4$ and $LiZnPO_4$:Ln^{3+}/Yb^{3+} (Ln = Ho, Er) phosphors.

FTIR

The FTIR spectra for the phosphors in the 400–4000 cm^{-1} spectral range are seen in Fig. 3. The non-doped and co doped 0.5% Er^{3+}/5% Yb^{3+}, $LiZnPO_4$:0.5% Ho^{3+}/3% Yb^{3+} nanophosphors have extreme bands peaking at 1100–960 cm^{-1}, which are assigned to the asymmetrical and symmetrical stretching modes of the P–O bond, respectively. The spectrum displayed a weak absorption band in the range 520–630 cm^{-1} which arises due to the P–O vibration mode.[36–38] The dopant of RE ions had little impact on the main structure of the matrix, according to the non-doped/co-doped FTIR spectra of several doped ions, which was compatible with the XRD data.

Optical characterization

Diffuse reflectance of $LiZnPO_4$:Er^{3+}, Ho^{3+}/Yb^{3+}. The reflectance spectrum of $LiZnPO_4$:0.5% Er^{3+}/5% Yb^{3+}, 0.5% Ho^{3+}/3% Yb^{3+} in the 380–1100 nm range are illustrated in Fig. S3.† The sharp pic in the NIR region at 980 nm can be assigned to the $^2F_{7/2} \rightarrow {}^2F_{5/2}$ electronic transitions of Yb^{3+}.[39] Therefore, doping Yb^{3+} ions is beneficial to enhance the up-conversion luminescence intensity and efficiency for $LiZnPO_4$:Er^{3+}, Ho^{3+}. The RE^{3+} activators create some heavy absorption lines. For example, those at ~379/521 nm are from the $^4I_{15/2} \rightarrow {}^4G_{11/2}/{}^2H_{11/2}$ transitions of Er^{3+} and those at ~363/451 nm belong to the $^5I_8 \rightarrow {}^5G_2/{}^5F_1$ transitions of Ho^{3+}.[39,40] Furthermore, the Kubelka–Munk function can be used to determine the magnitude of the band-gap

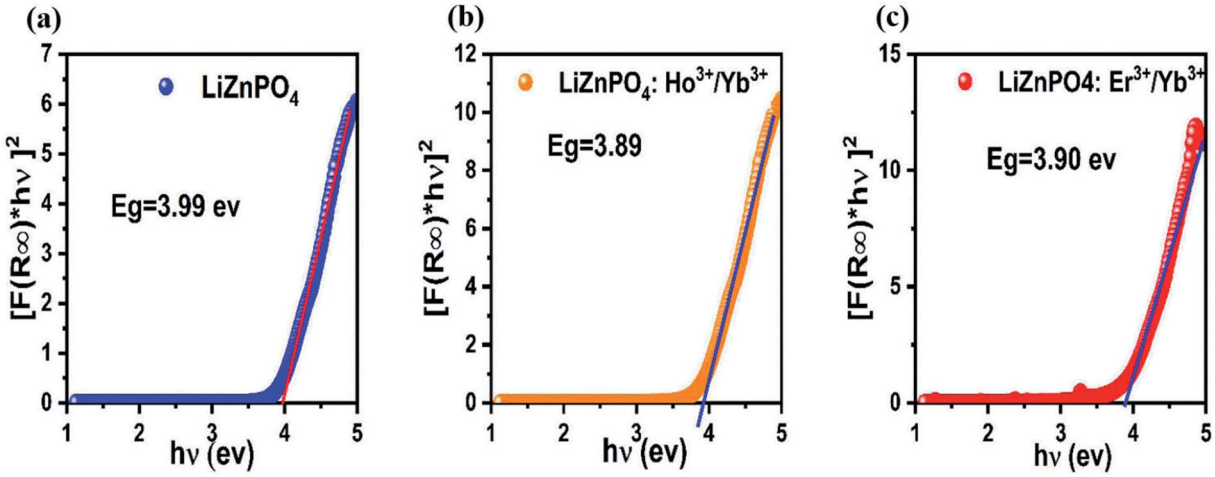

Fig. 4 Plot of $[F(R) \times h\nu]^2$ *versus* $h\nu$ for the band gap energy of $LiZnPO_4$, $LiZnPO_4$:Ho^{3+}/Yb^{3+} and $LiZnPO_4$:Er^{3+}/Yb^{3+}.

(E_g). This function was used to transform the measured reflectance into an analogous absorption range, which was normalized by the reflectance of the regular reference. As a result, the optical band-gap energy can be expressed as:[41]

$$(F(R) \times h\nu)^n = C(h\nu - E_g) \quad (1)$$

where $h\nu$ is the incident photon energy, C is a proportionality constant, and E_g is the band-gap (eV). The n is a factor that indicates whether or not an indirect transformation is possible for the n value 0.5 and whether or not a direct transition is allowed for the n value 2. The $(F(R) \times h\nu)^2$ *versus* on $h\nu$ is shown in Fig. 4a–c. The h value at the intersection of the tangent and the horizontal axis will be used to calculate the E_g for different samples. The E_g values are estimated as 3.99, 3.90 and 3.89 eV for $LiZnPO_4$, $LiZnPO_4$:Ho^{3+}/Yb^{3+} and $LiZnPO_4$:Er^{3+}/Yb^{3+}, respectively. This host broad bandgap efficiently accommodates the dopant ions energy levels to achieve luminescence.

The different crystalline morphology and size of the material based on different lanthanide ions could explain the differences in energy band gap values found for the doped and undoped phosphors.[42,43] This may also be explained by the presence of the Ho^{3+}, Er^{3+} and Yb^{3+} ions, which cause many defects in $LiZnPO_4$, inducing additional energy levels in the material band gap, so as to reduce the energy gap.

Concentration dependence of UCL

UCL of $LiZnPO_4$:0.5% Er^{3+}/x% Yb^{3+}. In order to analyze the effect of the Yb^{3+} ions concentration on the luminescent

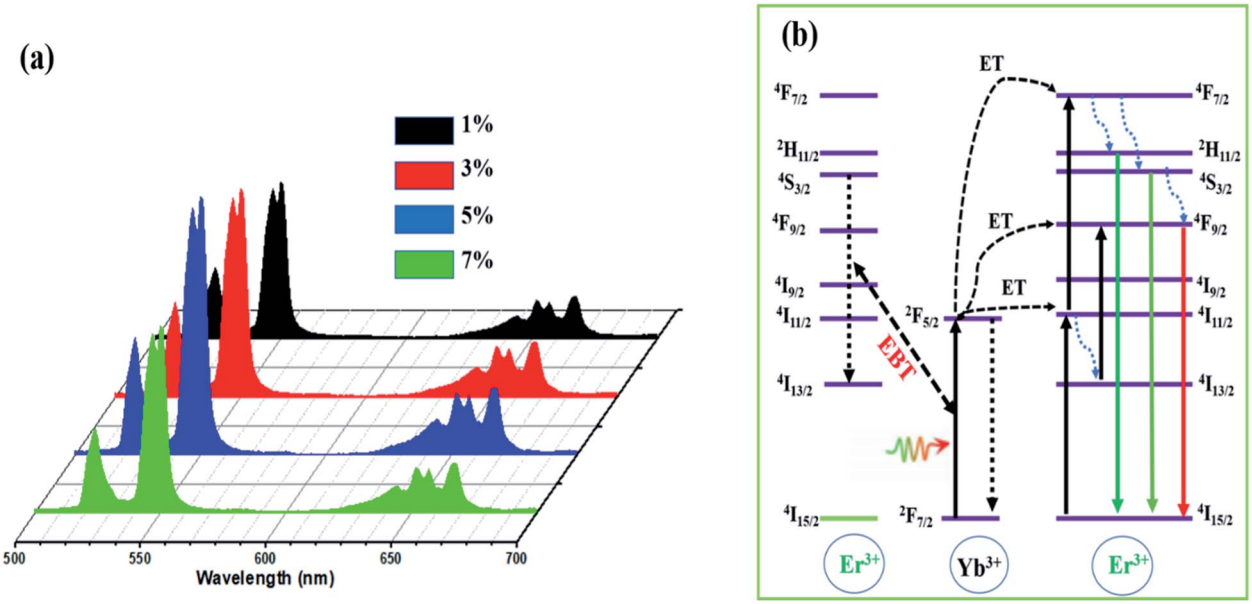

Fig. 5 (a) UC emission spectra of a series of $LiZnPO_4$:0.5% Ho^{3+}/x Yb^{3+} phosphors with different Yb^{3+} concentrations ($x = 1$, 3, 5 and 7 mol%). (b) Energy level diagram illustrating thermally promoted ET from Yb^{3+} to Er^{3+} ions.

properties, the room temperature UC emission spectra of $LiZnPO_4$:0.5 mol% Er^{3+}/x% Yb^{3+} nanophosphors were observed in the visible region with 980 nm excitation. Except for luminescent brightness, the as-prepared $LiZnPO_4$:Er^{3+}/Yb^{3+} present comparable spectral profiles, demonstrating that the crystal field around Er^{3+} ions is nearly similar and unaffected by changes in Yb^{3+} ion doping concentration. The UC emission spectra are made up of two green emission bands and a prominent red emission band, which come from Er^{3+} transitions $^2H_{11/2} \rightarrow {}^4I_{15/2}$ (524 nm), $^4S_{3/2} \rightarrow {}^4I_{15/2}$ (551 nm), and $^4F_{9/2} \rightarrow {}^4I_{15/2}$ (667 nm).[44] The green UC emission rate increases with the increase in Yb^{3+} ion concentration, attaining its maximum value at $x = 5\%$ (see Fig. 5a). As the doping concentration exceeds 5%, however, the emission rate begins to decrease. The Yb^{3+} ion has a high absorption cross section at 980 nm, as well as a large energy overlap between Yb^{3+} and Er^{3+} ions. As a consequence, energy can efficiently be transferred from Yb^{3+} ions to Er^{3+} ions, resulting in improved UC emission properties. Despite this, the UC emission rate demonstrated a downward trend as the Yb^{3+} ion concentration increased. This is mostly caused by the energy back transfer (EBT) from Er^{3+} to Yb^{3+} ions ($^4S_{3/2}$ (Er^{3+}) + $^2F_{7/2}$ (Yb^{3+}) → $^4I_{13/2}$ (Er^{3+}) + $^2F_{5/2}$ (Yb^{3+})).[45,46] Fig. 5b depicts the energy levels diagram of Yb^{3+}–Er^{3+} ions. The UC luminescence process of Er^{3+} has been thoroughly investigated in previous sources.[47,48] The existence of EBT from Er^{3+} to Yb^{3+} ions in the $LiZnPO_4$ phosphors can be also verified by measuring the decay curves (see Fig. S4†). A quadratic exponential function can be used to fit the temporal profile, and the average lifetime can be defined as:

$$\tau = (I_1 \times \tau_1^2 + I_2 \times \tau_2^2)/(I_1 \times \tau_1 + I_2 \times \tau_2) \quad (2)$$

On the basis of the fitting results, the average decay time for the $LiZnPO_4$:Er^{3+}/x Yb^{3+} crystals was revealed to be 190.34, 153.96, 125.56, and 83.18 μs, when the Yb^{3+} ion concentration was 1, 3, 5, and 7 mol%, respectively. The decreased in decay time value demonstrated the existence of EBT from Er^{3+} to Yb^{3+}.

Fig. 6a demonstrates the UC emission spectra of the $LiZnPO_4$ 0.5% Ho^{3+}/y% Yb^{3+} ($1\% \leq y \leq 7\%$) phosphors upon 980 nm excitation. All Ho^{3+}/Yb^{3+} codoped $LiZnPO_4$ phosphors released heavy red UC emissions. The emission bands at approximately 520–560 nm and 645–675 nm was assigned to ($^5F_4$, $^5S_2$) → $^5I_8$, and $^5F_5 \rightarrow {}^5I_8$, respectively. Both emission bands were in excellent accordance with previous researches on many other Ho^{3+} doped compounds.[40,49,50] The $^5F_5 \rightarrow {}^5I_8$ transition had the highest red emission of the two emission bands, resulting in a heavy red emission in Ho^{3+}/Yb^{3+} codoped $LiZnPO_4$ phosphors. The UC emission rate rose gradually with a Yb^{3+} rising concentration, reaching a height when the concentration of Yb^{3+} ($x = 3$ mol%) was 6 times than that of Ho^{3+}. The emission rate minimized when the Yb^{3+} concentration passed this critical value ($x = 3$ mol%). The UCL intensity diminishes owing to either the concentration quenching effect or the energy back transfer (EBT) mechanism from Yb^{3+} to Ho^{3+}.[51–54] Fig. 6b shows the energy level diagram of Yb^{3+}–Ho^{3+} in the $LiZnPO_4$ host. The detailed UCL process has been discussed in the recent work.[52] To have a better understanding of the mechanism of the UC emission process in Ho^{3+}/Yb^{3+} co-doped $LiZnPO_4$ phosphor, the normalized decay curves were presented in Fig. S5.† Using (eqn (2)), the average lifetime of $LiZnPO_4$:0.5% Ho^{3+}/y% Yb^{3+} ($y = 1$, 3, 5, and 7) from decay curves are estimed to be 81.35, 48.86, 33.44, and 19.42, respectively. This decrease is caused by the possibility of energy back-transfer (EBT) from Ho^{3+} to Yb^{3+}, which significantly improves the depopulation of the $^5F_4$, $^5S_2$ level and shortens the lifetime.

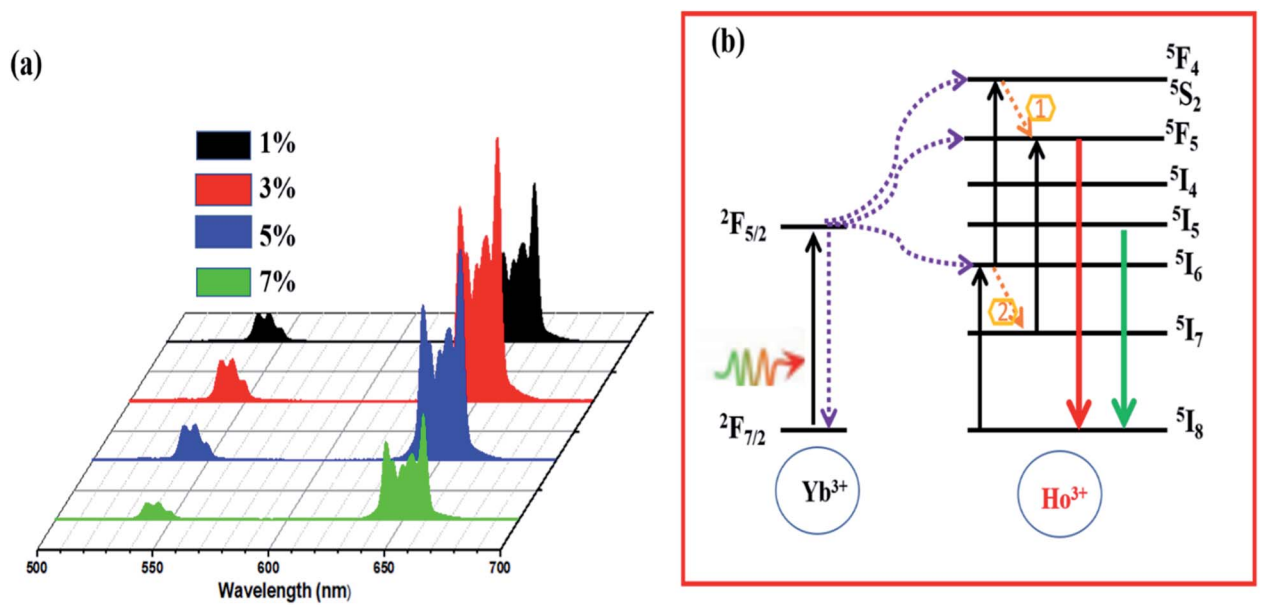

Fig. 6 (a) UC emission spectra of a series of $LiZnPO_4$:0.5% Ho^{3+}/y Yb^{3+} phosphors with different Yb^{3+} concentrations ($y = 1$, 3, 5 and 7%). (b) Energy level diagram illustrating thermally promoted ET from Yb^{3+} to Ho^{3+} ions.

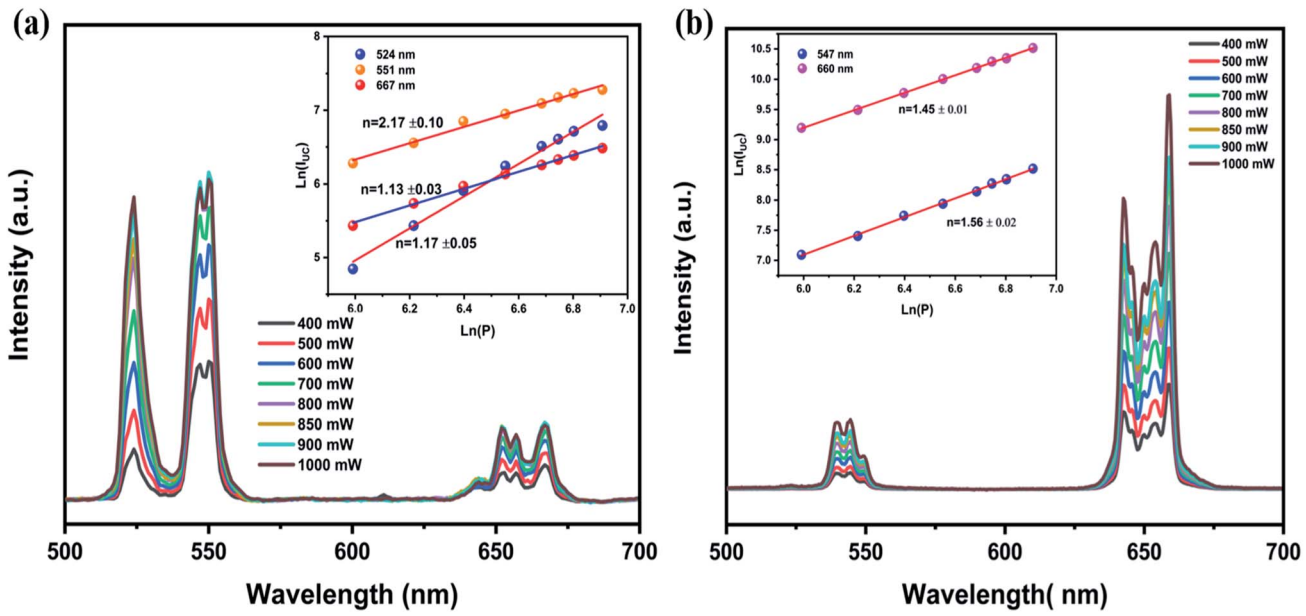

Fig. 7 Represents the variation UC emission at different pump powers, inset shows the dependences of ln(I_{UC}) on ln(P): (a) for LiZnPO4:Er^{3+}, Yb^{3+}. (b) For $LiZnPO_4$:Ho^{3+}/Yb^{3+}.

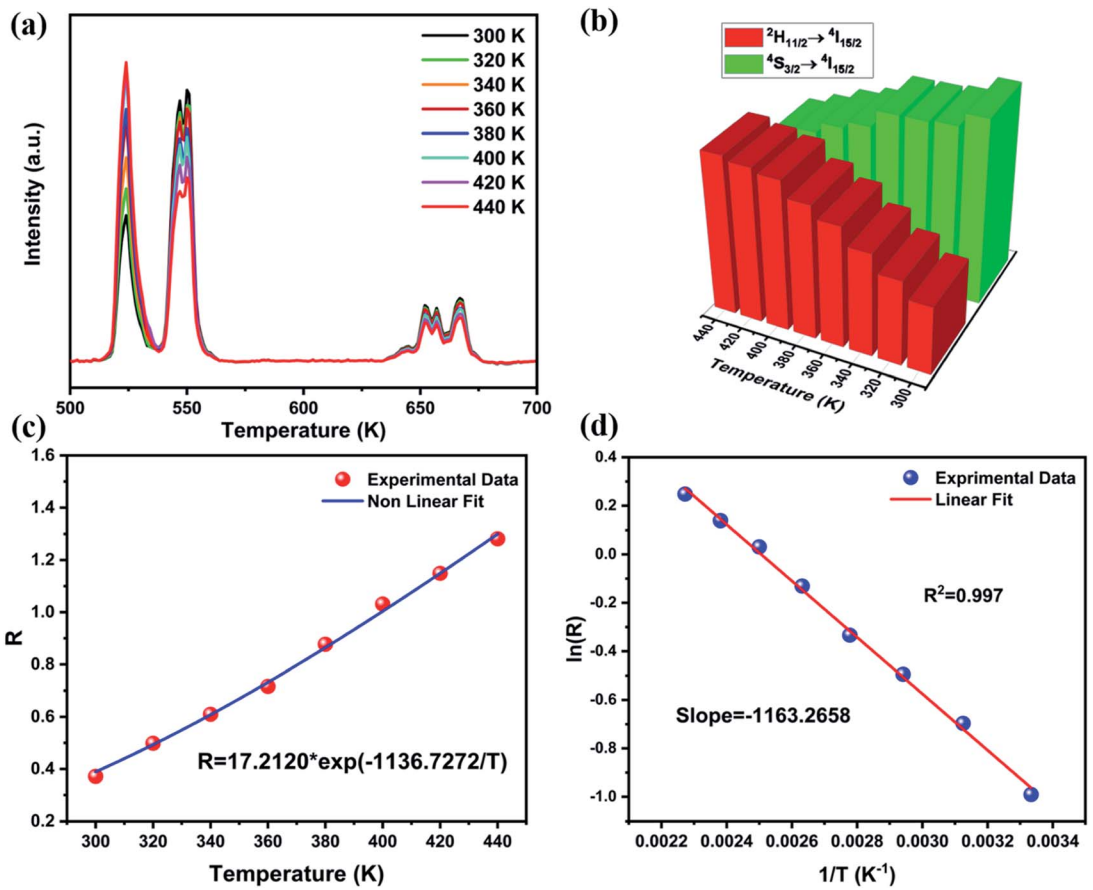

Fig. 8 (a) Temperature dependent spectra for LiZnPO4:0.5% Er^{3+}/5% Yb^{3+} samples; (b) luminescence intensity of the two thermal coupled levels at various temperature; (c) the R *versus* temperature and (d) the logarithm of ln(R) as a function of inverse absolute temperature (1/T).

Power dependence of UCL and luminescence mechanisms

To gain a better understanding of UCL processes and mechanisms, we investigate the relationship between up-conversion luminescence intensity (I_{UC}) and excitation power (P). The emission spectra of the $LiZnPO_4$:0.5% Er^{3+}/5% Yb^{3+} and $LiZnPO_4$:0.5% Ho^{3+}/3% Yb^{3+} sample as a function of excitation power are shown in Fig. 7a and b. With increased pump power, both green and red emissions for Er^{3+} and Ho^{3+} improve noticeably. The relationship between the UCL intensity (I_{UC}) and the pump power (P) is widely agreed to be as follows:[55]

$$I_{UC} \propto P^n \quad (3)$$

where n denotes the number of laser photons used to occupy the upper radiation level, and the slope of the fitted line denotes the slope of the fitted line. I_{UC} is UCL intensity and P is pump power. As displayed in the inset Fig. 7a and b. Similarly, the obtained n values for 524 nm, 551 nm, and 667 nm emissions in $LiZnPO_4$:Er^{3+}/Yb^{3+} nanoparticles are 1.17, 2.17, and 1.13, respectively. For $LiZnPO_4$:Ho^{3+}/Yb^{3+} system, the slopes of three fitting curves respectively corresponded to 547 nm and 660 nm emissions are 1.56 and 1.45. The results indicate that both $LiZnPO_4$:Er^{3+}, Ho^{3+}/Yb^{3+} systems are two-photon process.

Temperature sensing properties

The UC emission spectra were reported at different temperatures from 300 to 440 K upon 980 nm excitation at 450 mW to investigate the optical thermal sensing behavior of $LiZnPO_4$:-Yb^{3+}/Er^{3+} and exposed as Fig. 8a. The emission spectra change in lockstep with temperature, with the emission intensity of the $^4S_{3/2} \rightarrow {}^4I_{15/2}$ transition decreasing while the emission intensity of the $^2H_{11/2} \rightarrow {}^4I_{15/2}$ transition increasing as show in Fig. 8b. The $^2H_{11/2}$ and $^2S_{3/2}$ are the two thermally coupled levels.

As temperature of the phosphor sample increases, the overall emission intensity of the 521 and 554 nm emission bands decreases due to thermal quenching related to the increase of the ions lattice vibrations and thus non-radiative transitions. At 440 K, the relative intensity of the two emission bands changes accordingly and the emission intensity of the 521 nm band is larger compared to that of 554 nm band. The emission intensity variation is due to transfer of the excited ions from the lower to the upper thermally coupled levels *via* the lattice vibrations.[56,57]

Fig. 8c shows the FIR values of green emissions corresponding to the ($^2H_{11/2}$, $^4S_{3/2}$) thermally coupled levels to the ground state $^4I_{15/2}$ transitions, determined from the temperature-dependent PL emission spectra. The fluorescence intensity ratio of the thermally coupled levels emissions displays a remarkable increase with temperature increasing. According to the literature, one knows that the relative population of the thermally coupled levels follow the Boltzmann distribution with R parameter formulated as;[58]

$$R = \alpha e^{-\frac{\Delta E}{kT}} \quad (4)$$

where R is FIR for the 521 and 554 nm emissions of Er^{3+}, ΔE is energy difference between $^2H_{11/2}$ and $^4S_{3/2}$ levels of Er^{3+}, k is Boltzmann constant, T is absolute temperature and α is proportionality constant.

Fig. 8d exhibits a monolog plot of the R parameter of $LiZnPO_4$:Er^{3+}/Yb^{3+} from the $^2H_{11/2}$ and $^4S_{3/2}$ levels as a function of inverse absolute temperature in the 300–440 K range as representatives. The slope ($-\Delta E/k$) is a very critical parameter to find the optical temperature sensing ability of the luminescent material. The fitting of the experimental data creates the ΔE value of 808.46 cm^{-1}. This parameter can be affected by several variables, such as particle size, luminescent host lattice, doping concentration, excitation pump energy.[59–61] In order to study the influence of pump power on the sensor sensitivity, we looked at how the pump power affected the spectrum properties as a function of temperature. Fig. S6a and d† display UC emission spectra of $LiZnPO_4$ at 850 mW and 1000 mW at different temperatures. The FIR values change dramatically as the temperature rises, as seen in Fig. S6b–e.† Moreover, one notices at a constant temperature, the FIR values increase with the rise of pump power. This finding can be interpreted by the local heat

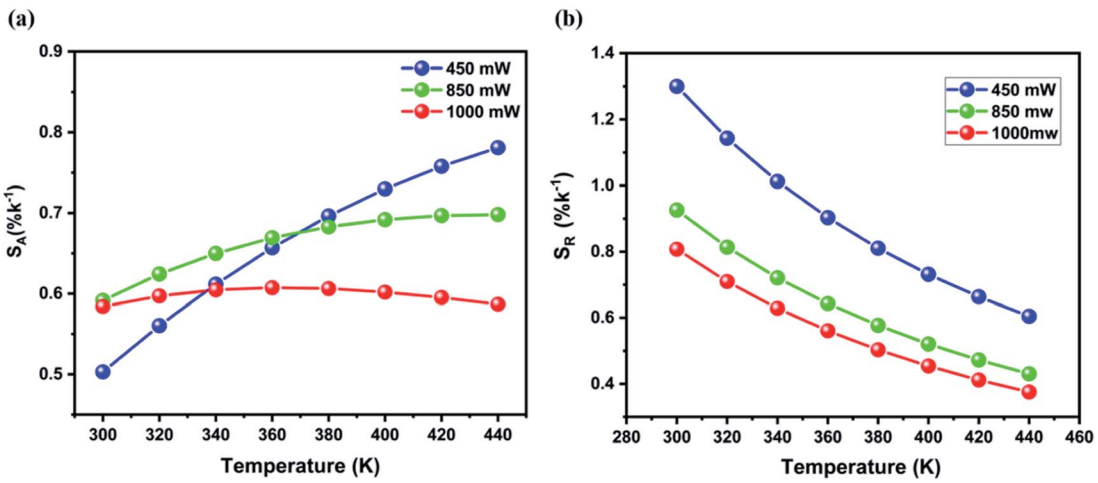

Fig. 9 (a) Absolute and (b) relative sensitivities of $LiZnPO_4$:Er^{3+}/Yb^{3+} as a function of temperature under different pump powers.

induced by 980 nm laser excitation. This high-powered laser will produce heat in the vicinity of the irradiation light spot in the sample, resulting in a temperature differential between the light spot and other regions. Fig. S6c and f† exhibit the ΔE values of 579.20 and 505.02 cm^{-1} for 850 and 1000 mW, respectively. Due to the presence of the local heat effect induced by the laser, we obtain a large difference value of ΔE compared to 808 cm^{-1}. According to the above study, the UC spectra excited at 450 mW causes the littlest heat effect, so it can be used for use in precise temperature sensing.

The sensor sensitivity of a temperature-sensing luminescent material is a critical factor in determining its application potential. According to ref. 62, absolute sensitivity (S_A) and relative sensitivity (S_R) can be determined using the following equation:

$$S_A(T) = R \times dR/dT \quad (5)$$

$$S_R(T) = 100 \times dR/dT \quad (6)$$

where R is the FIR of two emission peaks and T is absolute temperature.

According to the fitting results in Fig. 8b and S6† the absolute and relative sensitivities of $LiZnPO_4$:5% Yb^{3+}, 0.5% Er^{3+} for various pump powers were measured. Fig. 9a represents the absolute sensitivity as a function of temperature under pump powers of 450, 850, and 1000 mW. Based on the above results, it can be assumed that the energy difference ΔE and the constant D have a significant influence on the temperature detection range of the sensor.

The highest values of S_A are obtained to be about 0.614 (440 K), 0.658 (400 K), 0.620 (360 K) for 450, 850, and 1000 mW, respectively. Furthermore, the temperature value (T_{max}) with the highest sensitivity can be derived from eqn (3) by setting dS_A/dT to zero, as following formula:

$$T_{max} = \Delta E/2K_B \quad (7)$$

The high sensitivity maximum value S_{Amax} and the high temperature value T_{max} at various pump power are summarized in Table 1. Owing to the small range of temperature variation in the current study up to 440 K, the maximum has not been traced absolutely at 450 mW, but the maximum is predicted to occur at a much higher temperature. Furthermore, it's important to note that as pump power increases, the temperature at which the highest S_A value is found to decreases. The local heat effect also contributes to these phenomena.

Fig. 9b displays the relative sensitivities of the $LiZnPO_4$:5% Yb^{3+}, 0.05% Er^{3+} as a function of temperature under different pump powers. It can be noted that the relative sensitivity decreases with increasing temperatures for all pump powers, which is beneficial to the performance of temperature sensing applications. The best relative sensitivity is obtained upon 450 mW pump power. On the basis of the above study, it can be concluded that lower pump power is more advantageous to achieving higher overall sensitivity. The Er^{3+}/Yb^{3+} co-doped $LiZnPO_4$ sample exhibits a high relative sensitivity to a few reported temperature-sensing luminescent materials. Table 2 illustrated the optical temperature-sensing of Er^{3+}/Yb^{3+} co-doped other luminescent materials. In comparison with various phosphate matrices, a favorite result was achieved in the $LiZnPO_4$ co-doped Er^{3+}/Yb^{3+}. Furthermore, the sensitivity of the resultant was higher than the previously developed thermometer.

In addition, the equations below can be used to calculate the temperature resolution (T):[47]

$$\delta T = 1/S_R \times \Delta R/R \quad (8)$$

where $\Delta R/R$ is the sensitivity of the detection system, with a value, in our case of 0.5%.[47,69] Fig. 10 manifested the

Table 1 Values of S_{Amax} and T_{max} for Er^{3+}/Yb^{3+} $LiZnPO_4$ materials

Pump power	S_{Amax} (% K^{-1})	T_{max} (K)
450 mW	0.801	581
850 mW	0.691	416
1000 mW	0.594	363

Table 2 S_A and S_R parameters for serval optical temperature-sensing luminescent materials

Ln-ion	Matrix	Transitions	S_A (K^{-1})	S_R (% K^{-1})	Ref.
Er^{3+}	$K_3Y(PO_4)_2$	$^2H_{11/2}/^4S_{3/2}$	0.0034	1.2	63
Er^{3+}	$Sr_3(PO_4)_2$	$^2H_{11/2}/^4S_{3/2}$	0.0060	0.88	64
Er^{3+}	$NaZnPO_4$	$^2H_{11/2}/^4S_{3/2}$	0.0047	0.39	65
Er^{3+}	Ba_4BiF_{17}	$^2H_{11/2}/^4S_{3/2}$	0.0035	1.22	66
Ho^{3+}	$K_3Y(PO_4)_2$	$^5F_5/(^5F_4, ^5S_2)$	0.078	0.20	63
Ho^{3+}	$Sr_3Y(PO_4)_3$	$^5F_5/(^5F_4, ^5S_2)$	0.019	0.16	67
Ho^{3+}	$La_{9.67}Si_6O_{26.5}$	$^5F_5/(^5F_4, ^5S_2)$	**0.0226**	0.21	68
Er^{3+}	$LiZnPO_4$	$^2H_{11/2}/^4S_{3/2}$	**0.008**	1.29	This work
Ho^{3+}	$LiZnPO_4$	$^5F_5/(^5F_4, ^5S_2)$	**0.0229**	0.278	

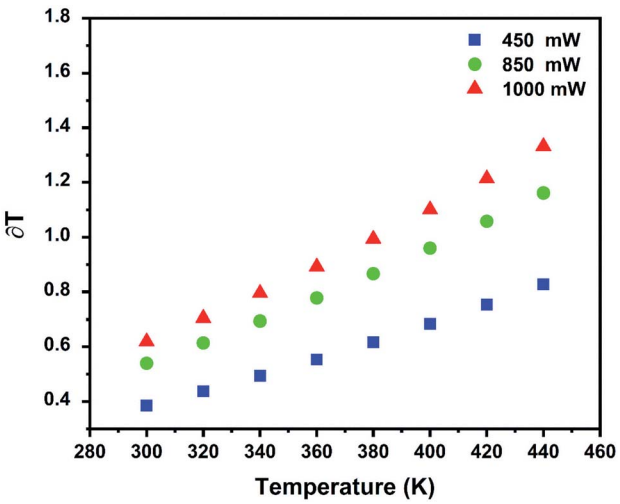

Fig. 10 Temperature uncertainty δT of $LiZnPO_4$:5% Yb^{3+}/0.5% Er^{3+} under different pump powers.

calculated values of temperature resolution at different pump power. At 450 mW power excitation, a remarkable low value of about 0.4 K was determined at 300 K and within the physiological temperature spectrum (commonly used IR cameras have a temperature instability of about 1 K at RT).[70] This value is smaller than 0.65 K reported for 850 mW and 1000 mW at 300 K. As the temperature rises, the thermal resolution is held below 1 K for all pump power up to 300 K, which is adequate for most applications.

Fig. 11a shows the emission spectra of the standard $LiZnPO_4$:3% Yb^{3+}/0.5% Ho^{3+} phosphor under 980 nm excitation with 450 mW at different temperatures. By rising temperatures, both green and red emissions are gradually weakened, as can be shown in Fig. 11b, which shows the relative intensity of the 545 and 657 nm emissions as function of temperature. The red emission intensity decreases at a slower rate than the green emission intensity. This may be due to the different population processes on the excitation states for the two emissions, as shown in Fig. 6b, which also show that the non-radiative relaxation (1) from the $^5I_6$ to the $^5I_7$ levels is very significant in the red UC emission phase. The R values dependence on absolute temperature is exhibited in Fig. 11c. The R value increases steadily as the temperature rises from 300 to 440 K, and the fitting of these experimental data yields a linear relationship:

$$R = 0.229 \times T + 1.429 \quad (9)$$

On the basis of eqn (3), the absolute sensitivity in the whole temperature range around 300 to 440 K is 0.02293 K^{-1}, which is considerably higher than that of many other Er^{3+}/Ho^{3+} doped luminescent compounds (see Table 2). The relative sensitivity determined by applying eqn (4) at different temperatures is presented in Fig. 11d. When the temperature rises from 300 to 440 K, the S_R decreases from 0.278% to 0.201% K^{-1}, respectively. It can be noticed that the S_R value is lower than those for Er^{3+} and higher for Ho^{3+} in unusual other luminescent materials as displayed in Table 2. Thus, further enhancement of S_R is still needed in the Ho^{3+}-activated $LiZnPO_4$ phosphor. Based on the above discussion, the Yb^{3+}–Er^{3+} co-doped $LiZnPO_4$ phosphor using TCLs exhibits the highest relative sensitivities in this study.

CIE coordinate and lifetime analysis

Fig. 12 display the Commission Internationale de l'Eclairclage (CIE) 1931 chromaticity coordinates from the UC emission spectra of Er^{3+}/Yb^{3+}, Ho^{3+}/Yb^{3+} codoped $LiZnPO_4$ phosphor samples at different temperature (300–440 K). As seen from the CIE diagram, at room temperature (300 K), the yellow color

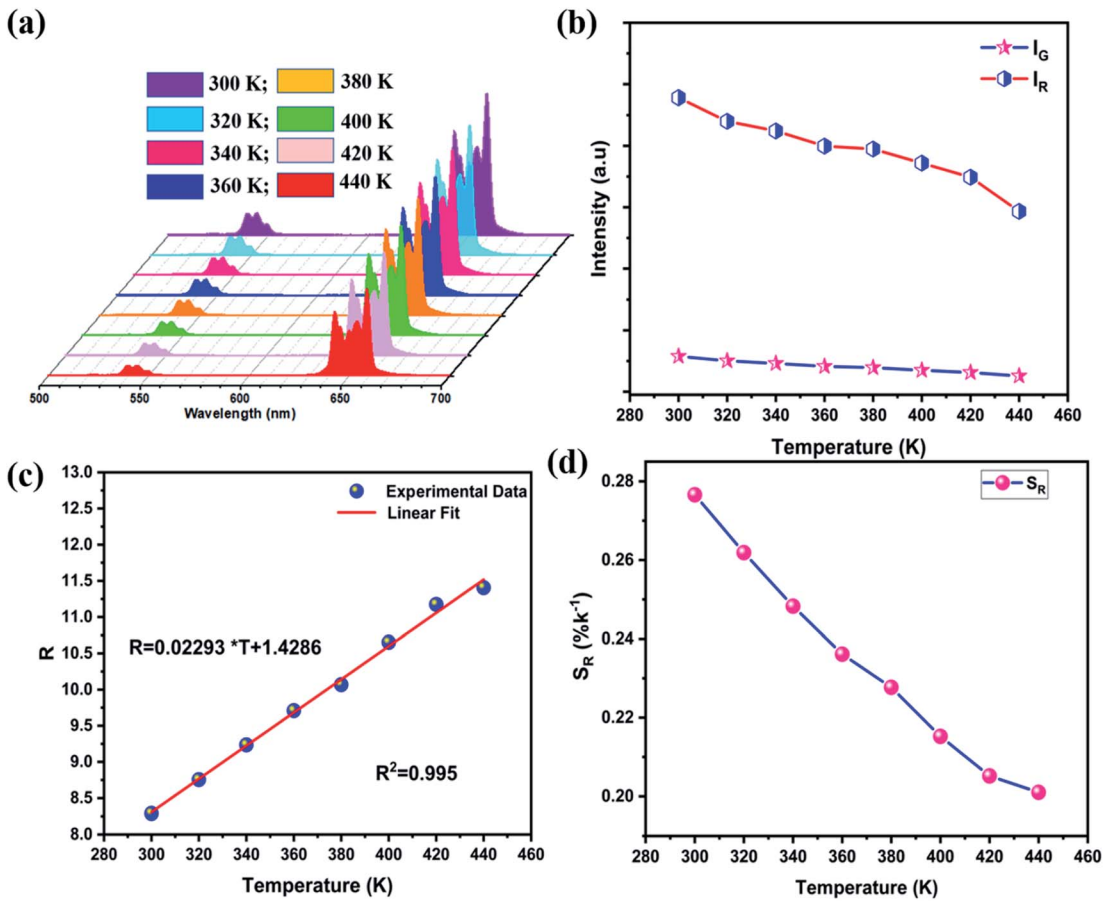

Fig. 11 (a) Temperature dependent spectra for $LiZnPO_4$:0.5% Ho^{3+}/3% Yb^{3+} samples; (b) luminescence intensity of the two non-thermal coupled levels at various temperature; (c) the R *versus* temperature and (d) dependence of relative sensitive (S_R) on absolute temperature presents.

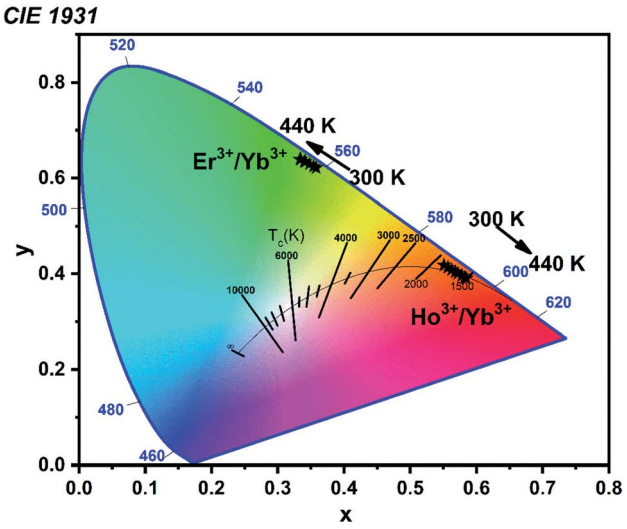

Fig. 12 Chromaticity coordinates of the emissions as a function of temperature.

perception with coordinates of (0.36, 0.62) was acquired, and after raising the temperature to 440 K, the color coordinates changed into the green region (0.31, 0.64) for Er^{3+} doped sample. For Ho^{3+} doped $LiZnPO_4$ phosphor, chromaticity coordinates shift from orange (0.54, 0.42) to reddish-orange (0.58, 0.38) region with increasing the temperature from 300 to 440 K.

Conclusions

In summary, the $LiZnPO_4$:Yb^{3+}–Er^{3+}/Ho^{3+} samples were prepared by sol–gel/Pechini method, and their luminescence characteristics for optical temperature sensing were investigated. As the RE ions are incorporated into the host lattice, the XRD study shows that the as-prepared samples are all single-phase. The pump-power-dependent UC spectra show that the Er^{3+}/Ho^{3+} emission peaks in the 500–700 nm range are a two-photon excitation process. Three primary emission peaks for Yb^{3+}–Er^{3+} doped $LiZnPO_4$ samples appeared in the visible region when excited at 980 nm, and the optimum Yb^{3+} doping concentration was found to be x = 5%. For the Yb^{3+}–Ho^{3+} codoped $LiZnPO_4$ samples, two emission peaks of Ho^{3+} were found, and the optimum Yb^{3+} doping concentration was found to be x = 3%. The Boltzmann distribution for FIR as a function of absolute temperature was obtained by thermally coupled levels of Er^{3+} in $LiZnPO_4$:Yb^{3+}/Er^{3+} phosphor. In comparison with various phosphate matrices, a favorite result was achieved in the $LiZnPO_4$ co-doped Er^{3+}/Yb^{3+} with $S_A = 0.008$ (K^{-1}) and $S_R = 1.29$ (% K^{-1}). On the other hand, FIR for the red and green emissions of Ho^{3+} were used to describe the temperature-sensing properties of Yb^{3+}–Ho^{3+} doped $LiZnPO_4$. The absolute sensitivity in the 300 to 440 K temperature range is 0.02293 K^{-1}, which is considerably higher than that of many other Er^{3+}/Ho^{3+} doped luminescent compounds. The relative sensitivity S_R decreases from 0.278% to 0.201% K^{-1}, by varying the temperature from 300 to 440 K respectively. These results demonstrate that $LiZnPO_4$ doped with Yb^{3+}/Er^{3+} and Yb^{3+}/Er^{3+} nanocrystals can be potential candidates for optical temperature sensing applications.

Conflicts of interest

There are no conflicts to declare.

References

1 P. M. Gschwend, F. H. L. Starsich, R. C. Keitel and S. E. Pratsinis, *Chem. Commun.*, 2019, **55**, 7147–7150.
2 C. Abram, B. Fond and F. Beyrau, *Prog. Energy Combust. Sci.*, 2018, **64**, 93–156.
3 I. E. Kolesnikov, M. A. Kurochkin, E. V. Golyeva, D. V. Mamonova, A. A. Kalinichev, E. Yu. Kolesnikov and E. Lähderanta, *Phys. Chem. Chem. Phys.*, 2020, **22**, 28183–28190.
4 M. Runowski, P. Woźny, S. Lis, V. Lavín and I. R. Martín, *Adv. Mater. Technol.*, 2020, **5**, 1901091.
5 X. Li, Y. Yu, J. Hong, Z. Feng, X. Guan, D. Chen and Z. Zheng, *J. Lumin.*, 2020, **219**, 116897.
6 J. Drabik and L. Marciniak, *ACS Appl. Nano Mater.*, 2020, **3**, 3798–3806.
7 A. M. Kaczmarek, M. Suta, H. Rijckaert, A. Abalymov, I. Van Driessche, A. G. Skirtach, A. Meijerink and P. Van Der Voort, *Adv. Funct. Mater.*, 2020, **30**, 2003101.
8 K. Trejgis, K. Maciejewska, A. Bednarkiewicz and L. Marciniak, *ACS Appl. Nano Mater.*, 2020, **3**, 4818–4825.
9 Y. Jiang, Y. Tong, S. Chen, W. Zhang, F. Hu, R. Wei and H. Guo, *Chem. Eng. J.*, 2020, 127470.
10 A. Shandilya, R. S. Yadav, A. K. Gupta and K. Sreenivas, *J. Mater. Sci.*, 2021, **56**, 12716–12731.
11 K. Binnemans, *Chem. Rev.*, 2009, **109**, 4283–4374.
12 K. Trejgis, A. Bednarkiewicz and L. Marciniak, *Nanoscale*, 2020, **12**, 4667–4675.
13 H. Huang, H. Zhou, J. Zhou, T. Wang, D. Huang, Y. Wu, L. Sun, G. Zhou, J. Zhan and J. Hu, *RSC Adv.*, 2017, **7**, 16777–16786.
14 A. Shandilya, R. S. Yadav, A. K. Gupta and K. Sreenivas, *Mater. Chem. Phys.*, 2021, **264**, 124441.
15 Monika, R. S. Yadav, A. Rai and S. B. Rai, *Sci. Rep.*, 2021, **11**, 4148.
16 A. Ishii and T. Miyasaka, *Adv. Sci.*, 2020, **7**, 1903142.
17 P. Singh, R. S. Yadav, P. Singh and S. B. Rai, *J. Alloys Compd.*, 2021, **855**, 157452.
18 K. Panigrahi, S. Saha, S. Sain, R. Chatterjee, A. Das, U. K. Ghorai, N. Sankar Das and K. K. Chattopadhyay, *Dalton Trans.*, 2018, **47**, 12228–12242.
19 A. S. Laia, D. A. Hora, M. V. d. S. Rezende, Y. Xing, J. J. Rodrigues, G. S. Maciel and M. A. R. C. Alencar, *Chem. Eng. J.*, 2020, **399**, 125742.
20 S. Liang, G. Li, P. Dang, Y. Wei, H. Lian and J. Lin, *Adv. Opt. Mater.*, 2019, **7**, 1900093.
21 J. Xue, M. Song, H. M. Noh, S. H. Park, B. C. Choi, J. H. Kim, J. H. Jeong and P. Du, *J. Alloys Compd.*, 2020, **843**, 155858.
22 J. Drabik and L. Marciniak, *J. Lumin.*, 2019, **208**, 213–217.

23 D. He, C. Guo, S. Jiang, N. Zhang, C. Duan, M. Yin and T. Li, *RSC Adv.*, 2015, **5**, 1385–1390.
24 I. E. Kolesnikov, A. A. Kalinichev, M. A. Kurochkin, E. Y. Kolesnikov and E. Lähderanta, *Mater. Des.*, 2019, **184**, 108188.
25 Y. Gao, F. Huang, H. Lin, J. Xu and Y. Wang, *Sens. Actuators, B*, 2017, **243**, 137–143.
26 W. Liu, X. Wang, Q. Zhu and J.-G. Li, *J. Alloys Compd.*, 2020, **829**, 154563.
27 J. Zhang, X. Jiang and Z. Hua, *Ind. Eng. Chem. Res.*, 2018, **57**, 7507–7515.
28 H. Zhang, Y. Liang, H. Yang, S. Liu, H. Li, Y. Gong, Y. Chen and G. Li, *Inorg. Chem.*, 2020, **59**, 14337–14346.
29 H. Dong, L.-D. Sun and C.-H. Yan, *Chem. Soc. Rev.*, 2015, **44**, 1608–1634.
30 C. Ouyang, S. Ma, Y. Rao, X. Zhou, X. Zhou and Y. Li, *J. Rare Earths*, 2012, **30**, 637–640.
31 X. Xiong, Z. Qiu and P. Li, *Mater. Today: Proc.*, 2020, **22**, 2544–2549.
32 S. A. Bhat, S. A. Ul Islam, M. Faizan and M. Ikram, *Optik*, 2019, **181**, 836–841.
33 L. Elammari and B. Elouadi, *Acta Crystallogr., Sect. C: Cryst. Struct. Commun.*, 1989, **45**, 1864–1867.
34 R. Shannon, *Acta Crystallogr., Sect. A: Cryst. Phys., Diffr., Theor. Gen. Crystallogr.*, 1976, **32**, 751–767.
35 A. A. Kaminskii, S. E. Sarkisov, T. I. Butaeva, G. A. Denisenko, B. Hermoneit, J. Bohm, W. Grosskreutz and D. Schultze, *Phys. Status Solidi A*, 1979, **56**, 725–736.
36 D. A. Hakeem and K. Park, *J. Nanosci. Nanotechnol.*, 2015, **15**, 5074–5077.
37 Z. Yahiaoui, M. A. Hassairi and M. Dammak, *J. Electron. Mater.*, 2017, **46**, 4765–4773.
38 K. Saidi and M. Dammak, *RSC Adv.*, 2020, **10**, 21867–21875.
39 A. K. Choudhary, A. Dwivedi, A. Bahadur and S. B. Rai, *J. Lumin.*, 2019, **210**, 135–141.
40 Monika, R. S. Yadav, A. Bahadur and S. B. Rai, *J. Phys. Chem. C*, 2020, **124**, 10117–10128.
41 K. Saidi and M. Dammak, *J. Solid State Chem.*, 2021, **300**, 122214.
42 A. Balakrishna and O. M. Ntwaeaborwa, *Sens. Actuators, B*, 2017, **242**, 305–317.
43 J. Massoudi, M. Smari, K. Nouri, E. Dhahri, K. Khirouni, S. Bertaina, L. Bessais and E. K. Hlil, *RSC Adv.*, 2020, **10**, 34556–34580.
44 P. Du, X. Huang and J. S. Yu, *Inorg. Chem. Front.*, 2017, **4**, 1987–1995.
45 J. Liao, Q. Wang, L. Kong, Z. Ming, Y. Wang, Y. Li and L. Che, *Opt. Mater.*, 2018, **75**, 841–849.
46 S. W. Yung, H. J. Lin, Y. Y. Lin, R. K. Brow, Y. S. Lai, J. S. Horng and T. Zhang, *Mater. Chem. Phys.*, 2009, **117**, 29–34.
47 N. M. Bhiri, M. Dammak, M. Aguiló, F. Díaz, J. J. Carvajal and M. C. Pujol, *J. Alloys Compd.*, 2020, **814**, 152197.
48 P. Du, L. Luo, X. Huang and J. S. Yu, *J. Colloid Interface Sci.*, 2018, **514**, 172–181.
49 X. Wang, X. Li, S. Xu, L. Cheng, J. Sun, J. Zhang and B. Chen, *J. Alloys Compd.*, 2018, **754**, 222–226.
50 S. Mondal, J. Sarkar, S. Panja, I. Dey, A. Sarkar, B. Ghosh, M. Kayal and U. K. Ghorai, *J. Phys. Chem. Solids*, 2019, **129**, 442–447.
51 T. Pang and Z. Huang, *Mater. Res. Express*, 2018, **5**, 066204.
52 A. Ali, H. Suo, Y. Wu, J. Xiang, X. Zhao and C. Guo, *Ceram. Int.*, 2019, **45**, 8428–8432.
53 P. Singh, R. S. Yadav and S. B. Rai, *J. Phys. Chem. Solids*, 2021, **151**, 109916.
54 R. S. Yadav and S. B. Rai, *J. Alloys Compd.*, 2017, **700**, 228–237.
55 R. Krishnan, S. G. Menon, D. Poelman, R. E. Kroon and H. C. Swart, *Dalton Trans.*, 2021, **50**, 229–239.
56 R. S. Yadav, D. Kumar, A. K. Singh, E. Rai and S. B. Rai, *RSC Adv.*, 2018, **8**, 34699–34711.
57 R. S. Yadav, S. J. Dhoble and S. B. Rai, *Sens. Actuators, B*, 2018, **273**, 1425–1434.
58 H. Zhang, S. Zhao, X. Wang, X. Ren, J. Ye, L. Huang and S. Xu, *J. Mater. Chem. C*, 2019, **7**, 15007–15013.
59 Y. Tian, Y. Tian, P. Huang, L. Wang, Q. Shi and C. Cui, *Chem. Eng. J.*, 2016, **297**, 26–34.
60 L. Peng, Q. Meng and W. Sun, *RSC Adv.*, 2019, **9**, 2581–2590.
61 M. Jia, Z. Sun, M. Zhang, H. Xu and Z. Fu, *Nanoscale*, 2020, **12**, 20776–20785.
62 J. Zhang and F. Qian, *Dalton Trans.*, 2020, **49**, 10949–10957.
63 J. Zhang, Y. Zhang and X. Jiang, *J. Alloys Compd.*, 2018, **748**, 438–445.
64 T. Zheng, L. Zhou, X. Qiu, D. Yang, M. Runowski, S. Lis, P. Du and L. Luo, *J. Lumin.*, 2020, **227**, 117517.
65 L. Mukhopadhyay and V. K. Rai, *New J. Chem.*, 2017, **41**, 7650–7661.
66 P. Liu, J. Liu, Y. Zhang, Z. Xia and Y. Xu, *J. Alloys Compd.*, 2020, **844**, 156116.
67 W. Liu, X. Wang, Q. Zhu, X. Li, X. Sun and J.-G. Li, *Sci. Technol. Adv. Mater.*, 2019, **20**, 949–963.
68 J. Zhang, J. Chen and Y. Zhang, *Inorg. Chem. Front.*, 2020, **7**, 4892–4901.
69 M. Back, E. Casagrande, C. A. Brondin, E. Ambrosi, D. Cristofori, J. Ueda, S. Tanabe, E. Trave and P. Riello, *ACS Appl. Nano Mater.*, 2020, **3**, 2594–2604.
70 M. Rodrigues, R. Piñol, G. Antorrena, C. D. S. Brites, N. J. O. Silva, J. L. Murillo, R. Cases, I. Díez, F. Palacio, N. Torras, J. A. Plaza, L. Pérez-García, L. D. Carlos and A. Millán, *Adv. Funct. Mater.*, 2016, **26**, 200–209.